Combustion analysis of a stratified pre-chamber ignition system by means of a zero-dimensional turbulence and flame speed model.

Macián, V., Salvador, F.J., De la Morena, J.*, Pagano, V.

CMT-Motores Térmicos, Universitat Politècnica de València, Camino de Vera s/n, 46022 Valencia (Spain)

Abstract

In the current work, the combustion process inside a stratified pre-chamber ignition system is analyzed. The pre-chamber is installed on a Rapid Compression-Expansion Machine (RCEM) and runs at different combinations of fuel-air equivalence ratio in the main chamber as well as in the pre-chamber, which is controlled by a fuel injection during the compression stroke. In order to analyze the results in detail, a zero-dimensional model for the pre-chamber is proposed. First, a K-k-ϵ model is developed and calibrated according to three-dimensional simulations in motoring conditions performed in a Computational Fluid Dynamic solver (Converge). Then, a thermodynamic model including the mass exchange between both chambers as wells as the heat transfer losses to the walls is used to compute the instantaneous heat release rate in the pre-chamber. Both pieces of information are combined to evaluate the effective flame propagation speed, and also to decouple the effects in terms of laminar flame speed, turbulence-flame interaction and gas velocity due to expansion effects in the burned products. The flame speed values obtained are consistent when the equivalence ratio in the pre-chamber is maintained, regardless the conditions in the main chamber, while a significant deterioration is seen once lean operation appears in the pre-chamber. Finally, the flame speed is compared to an average propagation speed estimated from broadband chemiluminescence visualization tests, showing good consistency with the model predictions.

Keywords: pre-chamber, turbulence, flame speed, heat release

*Corresponding author

Email address: joadela@mot.upv.es (De la Morena, J.)

1. Introduction.

Due to the increasing concern on global warming and climate change [1], researchers focused their attention on strategies to decrease fuel consumption and emissions in internal combustion engines. For direct-injection engines, multiple studies have analyzed the fuel injection operation, with the aim of analyzing the impact of the injector technology on its hydraulic performance [2, 3]. Other works have studied in detail the flow characteristics inside the injector, with particular focus of the nozzle [4], and its impact on the initial spray formation [5, 6]. In the case of spark-ignition engines, Banerjee et al. [7] studied the primary spray atomization. Pickett et al. [8] focused in the interaction between the different spray plumes, critical to understand the principles of the so-called spray collapse. Zeng et al. [9] studied the interaction between air flow and the gasoline spray development, while Peterson et al. [10] focused on the subsequent flame propagation.

In this sense, different kinds of numerical and experimental tools have been developed for the analysis of fuel injection and combustion processes. Simplified zero and one-dimensional models have been widely used to characterize macroscopic parameters [11, 12]. However, in the recent years more advanced methodologies such as Large Eddy Simulation (LES) [13, 14] and Direct Numerical Simulations (DNS) [15, 16] have been also used for the combustion analysis. Finally, different optical diagnostics [17, 18, 19] have also allowed the characterization of such processes from experimental side. The combination of all these techniques has proven to be a successful strategy for achieving a complete understanding of the complex phenomena involved with engine combustion.

Regarding the combustion strategies, several works explored low-temperature combustion modes based on autoignition of totally (Homogeneous Charge Compression Ignition) [20] or partially (Premixed Charge Compression Ignition) [21, 22] homogeneous mixtures. However, another way to accomplish these goals is operating the spark ignition engine under lean or diluted combustion mode [23, 24]. Nevertheless, such strategy opens many challenges on the ignition limits [25], the initial flame kernel development [26], the flame propagation [27, 28], and consequently on the combustion stability [29].

Pre-Chamber Spark Ignition (PCSI) system aims at overcoming these limits by replacing the spark plug with a small volume pre-chamber. The pressure rise due to the combustion development forces the pre-chamber active radicals and hot products to discharge through the nozzle into the main chamber [30] at high velocity. The turbulent jets entering the main chamber act as ignition sources, promoting fast burn rate of the charge thanks to the combination of high turbulence

intensity and multiple ignition points. Generally, the system is able to work under two different strategies: homogeneous or stratified mixture. In the first case, the pre-chamber is filled during the compression stroke with the homogeneous fuel-air mixture previously available in the main chamber. Under the stratified mode, an auxiliary fuel injection is done inside the pre-chamber during the compression to accurately control the equivalence ratio.

Attard et al. [31] demonstrated the potentiality of the PCSI system under stratified operation mode with different liquid and gaseous fuels. The combination of liquid gasoline (main chamber fuel) and gas propane (pre-chamber fuel) showed the best results in terms of leaner operation (maximum lambda at 2.1) while ensuring combustion stability. Attard et al. showed that the combustion system can also operate with a single fuel keeping high performance [32]. Furthermore, these experiments incorporated the variation of parameters such as the spark plug type, location, orientation and electrode gap. Results highlighted that only the spark plug depth slightly affected the capability to operate in lean conditions [33]. Coelho et al. [34] confirmed the system advantages, linked to a NOx, CO_2 and CO emissions reduction, although warned about an HC increase under ultra-lean strategies. Bunce et al. [35] and Korb et al. [36] performed optical and metal single-cylinder engine experiments to better understand the dynamics of interaction between both chambers. Jamrozik et al. [37] combined experimental tests on 2 stage PCSI engine powered with LPG gas with numerical simulations, providing data on spatial and temporal distributions of turbulent kinetic energy, pressure and temperature for different nozzle diameters. To fully understand how the PCSI system works, more basic studies have been performed on Rapid Compression Machines (RCM) [38] and Rapid Compression-Expansion Machines (RCEM) [39]. Gentz et al. identified the nozzle orifice as a critical parameter for the ejected jet shape and structure by carrying out optical tests varying the diameter of the orifices under the homogeneous [40] and stratified [41] strategies. They highlighted that only under stratified mode a significant extension of the ignition limits occurs. Gholamisheeri et al. [38] extended previous studies under leaner conditions linking Mach and Reynolds numbers with the jet penetration. Moreover, they completed the analysis combining numerical simulation results with experimental optical tests, analyzing pre-chamber mean velocity, turbulent kinetic energy and temperature fields [42, 43].

It is important to point out that all the benefits in terms of the flame speed, combustion time and ignition enhancement, mainly depend on the pre-chamber combustion process. Bardis et al. [44] developed a 0D model for pre-chamber gas engine modifying the energy cascade (K-k-ϵ)

equations from Fogla's turbulence model [45]. Their work took also into account the turbulent kinetic energy dissipation through the pre-chamber walls introduced by Borgnakke [46] and Achuth [47]. Furthermore, Bardis adapted Bargende's correlation [48] to improve the heat losses prediction by associating the characteristic velocity to the gas orifice velocity. Nevertheless, the analysis was limited to the compression stroke before combustion took place. Cruz et al. [49] developed a zero-dimensional code for the thermodynamic analysis of a pre-chamber ignition engine using Wiebe functions to replicate the heat release inside the pre-chamber. Hiraoka et al. [50] analyzed the pre-chamber induced combustion using a phenomenological 0D model using gas jet theory to evaluate the turbulence of the gas ejection from the pre-chamber. Bozza et al. [51] proposed a quasi-dimensional model for stratified pre-chamber engine, combining a geometrical model for the flame surface estimation with a previously developed combustion fractal model [52, 53]. The model has been validated against single-cylinder research engine results, showing good accuracy in terms of the pressure evolution in both chamber under several operating conditions.

In the current work, a zero-dimensional model for the evaluation of turbulence intensity, combustion velocity and heat release rate in the pre-chamber is developed. The model starts from Bardis' [44] K-k-ϵ turbulence model, with some adaptations based on the analysis of the flow field for the layout under investigation. The model constants are adjusted with the help of 3D-CFD simulations in motoring conditions (i.e. without the activation of the spark plug and subsequent combustion development). Then, the mode is coupled to a turbulent premixed flame model, adapted from the work of Kolla et al. [54] for spark-ignition engines, in order to evaluate the flame propagation inside the pre-chamber. The model results have been validated based on both the heat release rate analysis and broadband chemiluminescence visualization of the flames at the outlet of the pre-chamber orifices. The experimental matrix includes a variation of the fuel-air equivalence ratio in the pre-chamber (in the range of 0.9-1.1) as well as in the main one, covering lean (equivalence ratio 0.5) and ultra-lean (0.3) conditions.

As far as the paper structure is concerned, Section 2 thoroughly describes the experimental setup, including the details of the pre-chamber layout, the RCEM and the optical diagnostics used. The description of the 0D turbulent model and its tuning against 3D-CFD results in motoring conditions, including a sensitivity analysis to the parameters in the 0D model, is performed in Section 3. Section 4 presents the extension of the model to evaluate the turbulent premixed flame speed and the heat release rate in both chambers. The validation of this model against the visualization tests, and the

analysis of the influence of the boundary conditions in the combustion characteristics is performed in Section 5. Finally, the main conclusions are drawn in Section 6.

2. Experimental setup.

The experimental campaign has been performed in a Rapid Compression-Expansion Machine (RCEM) available in CMT-Motores Térmicos laboratory. In this section, the RCEM working principles, the equipment and instrumentation used, the test matrix and the methodology followed are described.

2.1. Rapid Compression-Expansion Machine (RCEM).

The RCEM is an experimental facility able to replicate the engine working process during the compression and initial expansion strokes, but allowing a better control of the boundary conditions. A sketch of the installation can be seen in Figure 1. The machine is composed of a set of pistons which are pneumatically driven, while an additional hydraulic circuit is introduced to couple these pistons and set some of the boundary conditions for the experiments.

Critical combustion parameters such as the compression ratio, the piston velocity (which can be expressed in terms of an equivalent engine speed), and the maximum distance between the cylinder head and the combustion piston can be adjusted by varying the oil and air volume. In this way, the system is able to replicate a wide range of engine layouts and different operating conditions.

The displacement piston controls the initial position of the combustion piston, while the pistons number 1 and 4 respectively control the compression stroke and allow the balance of the system inertial forces. The driver piston operates due to the pressure differential between the combustion and the driving chamber, and is hydraulically coupled to the piston 3 and mechanically coupled to the combustion piston. The combustion piston has a diameter of 84 mm, and its shape can be varied by changing the aluminum central part to mimic different engine hardware. Furthermore, it is possible to replace this aluminum part with a quartz window, allowing to perform optical tests. More details on the RCEM working process can be found in [55].

In terms of instrumentation, a Yokogawa DL850V high-frequency acquisition system (10 MHz) records the time evolution of pressure and main chamber volume, obtained by means of Kistler 6045A piezoelectric pressure transducers. These pressure sensors have been calibrated in the RCEM

in both static and motored conditions before the pre-chamber installation. The calibration constants have been adjusted to obtain the same pressure evolution for different thermodynamic conditions (initial pressure and temperature) and configuration (Compression Ratio). The instantaneous evolution of the piston position is recorded by means of an electromagnetic ruler and two AMO LMK102 incremental position sensors, with a resolution of 0.01 mm.

2.2. Combustion System Design.

In the current work, the original layout of the RCEM cylinder head has been modified replacing the spark plug housing with a pre-chamber, whose details can be seen in Figure 2.

The pre-chamber is screwed on the cylinder head to facilitate a quick switch between different pre-chamber geometries. The pre-chamber is mounted in the central position of the combustion chamber and houses the injector, spark plug and the piezoelectric pressure sensor. An NGK (LZK-RS 106 model) spark plug triggered by a multicharge Delphi ignition system, able to deliver around 80 mJ and 33 kV on maximum performance.

The pre-chamber is connected to the main chamber by means of 6 cylindrical orifices with 1.5 mm diameter and 2 mm length, equally distributed on the perimeter every 60° of revolution. The main chamber inlet angle (defined as the angle between the orifice axis and the pre-chamber axis) is around 60° for all the orifices. The pre-chamber volume is around 2.94 cm^3, i.e. approximately 4.5% of the total volume when the piston reaches top dead center.

2.3. Fuel Injection System

For the current study, iso-octane (C_8H_{18}) is used as a gasoline fuel surrogate. As mentioned during the introduction, the PCSI system operating under a stratified strategy needs an auxiliary injection in the pre-chamber to ensure optimal air/fuel mixture conditions during the spark plug activation. For this research, two single-orifice common-rail solenoid injectors, one for the main chamber and another one for the pre-chamber, have been selected and hydraulically characterized at CMT laboratory by means of an injection rate meter, based on Bosch's long tube method [56]. Both injectors are fed from a single high-pressure common-rail system. The injectors are driven by a Genotec trigger/pulse generator. To control low fuel injection quantity a small nozzle diameter around 0.090 mm has been chosen for the pre-chamber injector. Meanwhile, a bigger nozzle diameter around 0.156 mm is selected for the main chamber injection. The pre-chamber injection timing has

been adjusted at a piston position of 87 mm in order to ensure high enough density in the pre-chamber to avoid wall-wetting issues but maintaining some time for fuel evaporation and mixing process.

2.4. Broadband chemiluminescence visualization

The transition of the flames from the pre-chamber to the main one, as well as the subsequent combustion development, have been studied by means of a broadband chemiluminescence visualization technique. For this purpose, the central part of the combustion piston has been replaced by a quartz window, making it possible the visualization from the bottom of a 46 mm diameter section out of the total 84 mm bore. Regarding the optical equipment, a Photron's SA-Z high-speed camera records the images with a temporal resolution of 0.1 MHz (time step of 10 μs), achieving a spatial resolution of 6.5 $pixels/mm$. Since the chemiluminescence intensity produced by premixed lean combustion is low, a high speed gated image intensifier (C1088003F model) is used. A UV-Nikkor 105 mm f/4.5 lens is coupled with the intensifier allowing to capture a broadband light emission (between 220 and 900 nm).

2.5. Experimental Boundary Conditions

In this section, the experimental matrix will be described. First of all, it is important to underline that to evaluate the methodology repetitiveness, every single test is replicated 10 times. All these experiments are performed under the same initial conditions and parameters. Initial pressure and temperature are fixed on 0.15 MPa and 365 K, respectively. The maximum distance between the cylinder head and the combustion piston is equal to 120 mm and the driving gas pressure is set around 2.2 MPa. These parameters lead to a compression ratio and an equivalent engine speed around 11:1 and 1500 rpm, respectively. In order to ensure homogeneous conditions at the test beginning, the filling process and the main injection are performed 1 minute before the slow compression runs. The pre-chamber auxiliary injection trigger is activated by the piston position during the fast compression. In this analysis, the pre-chamber equivalence ratio impact on combustion is under investigation by means of auxiliary injection duration sweep. Indeed the air/fuel ratio in the pre-chamber is controlled by the amount of the injected fuel, depending on the main chamber's initial equivalence ratio. Table 1 summarizes the experimental matrix. Moreover, a flat piston shape is chosen in order to minimize the effects on the geometry into the turbulence field in the main chamber.

Table 1: Main chamber and pre-chamber fuel injected mass

ϕ_{mc} [-]	$m_{f,mc}$ [mg]	ϕ_{pc} [-]	$m_{f,pc}$ [mg]
0.5	33.1	1.1	1.9
0.5	33.1	0.9	1.3
0.3	19.9	1.1	3.3
0.3	19.9	0.9	2.0

3. Turbulence modeling without combustion.

The current section describes the numerical models and methodologies used to evaluate the turbulence evolution inside the pre-chamber in motoring conditions. First, the three-dimensional CFD model used for the characterization of the turbulence inside the pre-chamber is described. In particular, the mesh characteristics, boundary conditions and numerical methods selected for this purpose are summarized. The results of this 3D simulation are the baseline to adjust a zero-dimensional K-k-ϵ turbulence model for the pre-chamber, which is described next. The model includes a compressible nozzle equation that calculates the mass transfer and the velocity through the orifices communicating the pre-chamber and the main chamber based on the instantaneous pressure evolution, which is the most relevant source for turbulent kinetic energy generation. Finally, a sensitivity analysis of the main parameters of the 0D model, and the final comparison against the full 3D-CFD results are performed.

3.1. 3D-CFD simulations.

The mass flow exchange and turbulence generation inside the pre-chamber during the compression stroke are first determined by means of a 3D-CFD simulation in Converge [57]. In order to do so, a detailed mesh of the geometry used for the experiments (further described in Section 2), starting from the piston position at the start of the experiment (at 120 mm distance from the cylinder head) is generated.

Once the simulation starts, the temporal evolution of the piston position acquired (depicted in figure 3) from a motoring test at a 11:1 compression ratio, an initial pressure of 0.15 MPa and an initial temperature of 365 K are imposed. The main chamber is initialized with an equivalence ratio 0.5 mixture of air and fuel (iso-octane), representative of an early injection before the rapid compression starts. Instead, the pre-chamber is assumed to be filled initially with air. The turbulence is modeled by means of a Unsteady Reynolds-Averaged Navier-Stokes (U-RANS) strategy, in

particular using the so called Rapid Distortion Re-Normalization Group (RNG) $k-\epsilon$ model, with a second-order upwind numerical scheme. Since the experiments starts with the piston stopped at its minimum position, so there is no flow in the orifices of the pre-chamber, the turbulent kinetic energy (k) and turbulent dissipation (ϵ) are initialized at small values of 1 m^2/s^2 and 100 m^2/s^3, respectively, to take into account the residual flow from the filling process of the cylinder before the experiment starts. Other physical parameters (pressure, temperature, velocity, etc.) are solved with a MUSCL second order scheme and using the Pressure Implicit with Splitting of Operators (PISO) method for convergence.

One of the most important aspects in the modeling of the pre-chamber flow is related to the mesh characteristics. In particular, the mesh structure and size inside the orifices connecting both volumes (main chamber and pre-chamber) are critical, since the velocity in these orifices is deemed to be the main driver for turbulence generation inside the pre-chamber. Additionally, it is necessary to properly capture turbulence dissipation both inside the flow and around the pre-chamber walls.

In the current simulations, three different conditions for the mesh are imposed after a mesh sensitivity analysis:

- The parameter "base grid" represents the initial size of the mesh inside the main chamber. Based on previous experiences in the literature [43, 58], a value of 4 mm is selected.

- From the base size, a mesh refinement is performed in the walls and volumes corresponding the orifices and the pre-chamber using the embedding tool, in order to ensure that the mesh in these critical parts of the geometry is fine enough to capture the main flow features. In particular, a five level refinement is applied to the orifices and the pre-chamber volume, reaching a value of 0.125 mm. In the walls of the orifices, the refinement was done with one step more, leading to a minimum cell size of 0.0625 mm.

- Finally, an Adaptive Mesh Refinement (AMR) criteria is imposed, where the mesh is refined as long as a gradient of 0.1 m/s between adjacent cells is reached, again with a minimum value of 0.0625 mm.

In order to find these values, a mesh sensitivity analysis was preliminary performed. This information is presented in Figure 4 in terms of the evolution of the total mass inside the pre-chamber during the compression stroke. This mass is mainly a consequence of the velocity through

the orifices, which is affected by the quality of the mesh in the orifices and their vicinity. For this reason, the number of cells is changed by inducing variations in the embedding and AMR parameters, while the base cell size inside the main chamber is kept constant. As it can be seen, the pre-chamber mass always increases as a finer mesh is used. However, it has to be considered that the variation between the final two meshes is small, while further refinement of the mesh would imply a significant increase in computational cost. For this reason, the decision was to proceed with the last of the configurations presented, leading to a total of approximately 1.8 million cells at the spark timing. The structure of the chosen mesh around one of the orifices can be seen in Figure 5.

Finally, the results of the simulations are validated against the experimental operation of the RCEM in Figure 6. In this chart, the evolution of the pressure in the main chamber is depicted in blue color, while the pressure in the pre-chamber is shown in orange. Additionally, the experimental trace is presented in continuous lines, while dash lines are used for the modeled results. As it can be seen, there is almost a perfect match of the evolution both at the start of the rapid compression as well as in the vicinity of Top Dead Center (which is the most relevant region, since it is when the combustion in the pre-chamber takes place). However, between 12 and 16 ms there is a slight underestimation of the pressure evolution. It has to be noted that this region corresponds to the maximum piston velocity operation. On the one hand, higher velocity means higher uncertainty in the piston position acquisition and, on the other hand, the piston is more subjected to mechanical deformations induced by inertial terms [59, 60]. The pressure ratio between main chamber and pre-chamber (depicted on the bottom side of figure 6), which is the physical parameter driving the velocity through the orifices, is anyway almost equal to the experiments along the complete simulation (maximum deviation less than 1%).

3.2. Zero-dimensional turbulence model.

In order to perform a detailed analysis of the combustion development in the pre-chamber, it is necessary to evaluate separately the effects from the pre-chamber composition and the thermodynamic conditions (mostly temperature and pressure), included in the laminar flame speed, as well as the interaction of the flame development with the turbulent flow. For this purpose, a 0-D turbulence model is evaluated. The main source for the turbulence is the velocity of the gas exchange between chambers, calculated based on a compressible nozzle equation.

The turbulence model validated in the current paper is adapted from the $K-k-\epsilon$ formulation proposed by Fogla et al. [45] for the calculation of the turbulence induced by tumble motion in

spark-ignition engines, and adapted by Bardis et al. [44] for pre-chamber systems.

In this model, the following equations are considered:

$$\frac{\partial(m_{pc}K)}{\partial t} = P_{uK} - P_{kl} \tag{1}$$

$$\frac{\partial(m_{pc}k)}{\partial t} = P_{uk} + P_{kl} + P_{sw} - m_{pc}\epsilon - F_{wk} \tag{2}$$

$$\frac{\partial(m_{pc}\epsilon)}{\partial t} = P_{u\epsilon} + P_{\epsilon} + P_{sw}\frac{\sqrt{k}}{L_{pc}} - \frac{1.921 \cdot m_{pc}\epsilon^2}{k} - F_{w\epsilon} \tag{3}$$

Where K is the kinetic energy inside the pre-chamber, k the turbulent kinetic energy, ϵ the turbulence dissipation, m_{pc} is the mass in the pre-chamber, t is the time, the term P_{uX} is the production source term on each equation related to the flow entering through the orifices (being X the turbulent kinetic energy or dissipation, depending on the equation considered), P_{kl} corresponds to the conversion of kinetic energy into turbulent kinetic energy, P_{sw} is a production term on each equation induced by a swirl flow inside the pre-chamber, F_{wX} a dissipation term by viscous friction close to the walls, L_{pc} the Taylor's macroscale and P_{ϵ} represents the source of dissipation from the main pre-chamber flow.

However, compared to the work by Bardis et al. [44] the following simplifications have been made:

- Since the orifices point to the center of the pre-chamber, it is assumed that the structure of the flow does not induce any swirl-like vortices, so the term P_{sw} is neglected.
- Based on a previous sensitivity analysis, and considering the low rugosity of the internal walls of the pre-chamber, the turbulence dissipation term in the walls F_{wX} is considered small compared to the standard dissipation. Therefore, only one dissipation term (corresponding to ϵ) is included.
- Taylor's macroscale in the pre-chamber L_{pc} is considered to be proportional to the pre-chamber height h_{pc} ($L_{pc} = C_{len} \cdot h_{pc}$).

The terms corresponding to the contribution of the flow through the orifices on each equation (P_{uK}, P_{uk} and $P_{u\epsilon}$) are calculated taking into account the mass flow ($\dot{m}_{ori}$) and velocity (u_{ori}) in the orifices connecting both chambers:

$$P_{uK} = (1 - a_{in})(1 - C_T) \cdot \frac{1}{2} \sum_{n_{ori}} \dot{m}_{ori} u_{ori}^2 \tag{4}$$

$$P_{uk} = a_{in}(1 - C_T) \cdot \frac{1}{2} \sum_{n_{ori}} \dot{m}_{ori} u_{ori}^2 \tag{5}$$

$$P_{u\epsilon} = a_{in}(1 - C_T)C_\epsilon \cdot \frac{1}{2} \sum_{n_{ori}} \frac{u_{ori}}{D_{ori}} \dot{m}_{ori} u_{ori}^2 \tag{6}$$

In these equations, the terms a_{in} and C_ϵ represent the fraction of the kinetic energy of the incoming flow that contributes directly to turbulence generation and dissipation, respectively; C_T is a geometric coefficient related to the inclination of the orifices with respect to the pre-chamber axis; n_{ori} represents the number of orifices; D_{ori} the diameter of these orifices; and $\dot{m}_{ori}$ and u_{ori} are the mass flow and velocity in the orifices, calculated from the pressure ratio across the orifices through a compressible nozzle equation under subcritical conditions:

$$\dot{m}_{ori} = C_d A_{ori} \left(\frac{p_{out}}{p_{in}}\right)^{\left(\frac{1}{\gamma}\right)} \sqrt{\rho_{in} p_{in} \frac{2\gamma}{\gamma - 1} \left[1 - \left(\frac{p_{out}}{p_{in}}\right)^{\frac{\gamma-1}{\gamma}}\right]} \tag{7}$$

Where the subscripts *in* and *out* represent the conditions in the chambers from which the flow comes and where the flow arrives, respectively, γ is the adiabatic coefficient, A_{ori} the transversal section of each orifices (independent on the flow direction since the orifice is cylindrical) and C_d is the orifice discharge coefficient. This parameter has been set according to steady-state flow simulations at different pressure ratio conditions, reaching to the following formulation when the flow enters into the pre-chamber:

$$C_{d,fil} = 0.655 - \frac{0.095}{\sqrt{Re}} \tag{8}$$

while when the discharge from the pre-chamber to the cylinder takes place, the discharge coefficient is calculated as:

$$C_{d,dis} = 0.7 - \frac{0.127}{\sqrt{Re}} \tag{9}$$

It has to be considered that, although the mass transfer is calculated for the complete experiment, the corresponding production terms in the $K-k-\epsilon$ model equations are only active when the flow is incoming into the pre-chamber. Instead, when the discharge is initiated, the pre-chamber will lose kinetic energy and turbulence as a consequence of the mass drop.

Finally, the equations for the calculation of the terms P_{kl} and P_ϵ are described below:

$$P_{kl} = C_\beta \nu_T \frac{2m_{pc}K}{L_{pc}^2} - \frac{2}{3}m_{pc}k\left(\frac{\dot{\rho}_{pc}}{\rho_{pc}}\right) - \frac{2}{3}m_{pc}\nu_T\left(\frac{\dot{\rho}_{pc}}{\rho_{pc}}\right)^2 \tag{10}$$

$$P_\epsilon = \frac{\epsilon}{k}\left[5.76 C_\beta \nu_T \frac{m_{pc}K}{L_{pc}^2} - 2m_{pc}k\left(\frac{\dot{\rho}_{pc}}{\rho_{pc}}\right) - \frac{2.64}{3}m_{pc}\nu_T\left(\frac{\dot{\rho}_{pc}}{\rho_{pc}}\right)^2\right] \tag{11}$$

where C_β is a constant representing the fraction of kinetic energy inside the pre-chamber that is transformed into turbulence, ν_T is the turbulent viscosity, estimated as $0.09\frac{k^2}{\epsilon}$ consistently to the methodology used in the 3D-CFD simulations, ρ_{pc} is the average density in the pre-chamber and $\dot{\rho}_{pc}$ is the temporal derivative of this average density.

3.3. Model constants adjustment and sensitivity analysis.

From the development of the aforementioned equations, four constants need to be adjusted depending on the particular pre-chamber layout used:

- a_{in}, representing the amount of the kinetic energy of the inlet flow that is contributing to turbulence in the pre-chamber.
- C_β, which accounts for the conversion of average kinetic energy inside the pre-chamber to turbulence.

- C_ϵ, accounting for the turbulence dissipation as a consequence of the incoming flow into the pre-chamber.
- C_{len}, used to estimate Taylor's macroscale from the pre-chamber height.

Constant	**Range**	**p-value**	**Optimized**
a_{in}	[0.1 0.7]	0.0002	0.3
C_β	[0.1 0.7]	0.047	0.2
C_ϵ	[0.01 0.1]	0.0000	0.03
C_{len}	[0.2 0.7]	0.049	0.57
$R^2 adjusted$		87.51%	

Table 2: Analysis of Variance and optimization.

In order to adjust these constants, a surface response model and optimization process has been performed in the statistical software Statgraphics Centurion XVII [61]. For this purpose, and taking into account the low computational effort required to run the 0D model, a full factorial design with five levels per variable has been selected, resulting in a total of 625 combinations. The merit function from the optimization used to evaluate the capability of the model was the sum of the squared errors, calculated from the deviation between the 0D and 3D models in terms of the temporal evolution of the average turbulent kinetic energy in the pre-chamber. As a first step, an Analysis of Variance (ANOVA) technique was used to identify the sensitivity of the model to the different constants. Then, the surface response model was created using quadratic functions and used to look for the coefficients that could minimize the error. All this information is summarized in Table 2. In this table, the third column (p-value) is related to the significance of each model constant into the merit function, with a value of 0.05 indicating that this constants impacts the result with a 95% confidence. As it can be seen, the most significant parameters are a_{in} and C_ϵ, since the p-value obtained is close to zero. Instead, the impact of C_β and C_{len} is much lower, although still significant considering the threshold of 95% confidence selected. It has to be noted that the value of C_{len} is close to 0.5, which means that Taylor's macroscale is close to half the pre-chamber height, which is consistent with the flow structure previously seen. Additionally, the adjusted R-squared value of 87.51% indicates that the response surface model used for the optimization is capable of reproducing the error trends with a reasonable accuracy.

The result of the 0D model with the optimized constants has been evaluated against the 3D-

CFD results in Figure 7 up to Top Dead Center (TDC). In this chart, the continuous line represents the 0D model and the dashed line the 3D-CFD reference. In addition,a dual x-axis is utilized to indicate both the time elapsed (bottom side) since the start of the test and the piston position (top side) associated with the time evolution (from this moment on, the piston position has been always shown where considered necessary). It can be observed how both models match almost perfectly during the complete compression stroke. A vertical dotted line representing the top dead center in the experimental campaign has been inserted as a reference.

Figure 8 shows the sensitivity to all the model constants around this optimal solution. For this purpose, a variation of $\pm 25\%$ over the final value of each coefficient has been performed. As it was expected from the previous ANOVA analysis, the results are very sensitive to the variations in a_{in} and C_ϵ, while almost no effect is observed when changing the other two.

4. Combustion modeling.

This section is dedicated to the main and pre-chamber thermodynamic models under fired (combustion) conditions. This includes the thermodynamic model used to calculate the heat release rate from the instantaneous pressure analysis in both the pre-chamber and the rest of the cylinder, as well as the extension of the zero-dimensional turbulence model used to estimate the flame speed in the pre-chamber.

4.1. Heat release rate analysis.

The equations that govern the PCSI system will be discussed in order to better understand the combustion events. The following simplifications are considered:

- The thermodynamic model is constructed on a single-zone for the main chamber and pre-chamaber volumes, while burned and unburned thermodynamic propreties are estimated for the pre-chamber to predict the flame propagation speed.
- Mechanical deformations (which affect the instantaneous volume) are considered only for the main chamber.
- Blow-by leakages are neglected. Leakages have been previously evaluated by inducing different pressure values in the combustion chamber with the piston locked at its minimum position, producing less than 0.2 bar/min at the maximum combustion chamber pressure.

- The composition of the burned products in both chambers is estimated assuming a single-step reaction mechanism as a function of the equivalence ratio.

According to the previous hypotheses, the heat release rate in the main chamber can be calculated based on the first law thermodynamics for an open system:

$$HRR_{MC} = \frac{C_{P,MC}}{R} P_{MC} \frac{dV_{MC}}{dt} + \frac{C_{P,MC}-R}{R} V_{MC} \frac{dP_{MC}}{dt} + \dot{Q}_{MC,loss} + \dot{m}_{ori} h_{ori} \tag{12}$$

where $C_{P,MC}$ is the constant pressure specific heat of the main chamber mixture, R is the perfect gas constant, V_{MC} is the main chamber volume (function of the piston position and the mechanical deformations), dP_{MC} is the pressure rate, $\dot{Q}_{MC,loss}$ is the heat transfer through the main chamber walls, $\dot{m}_{ori}$ is the mass flow rate through the nozzle, and h_{ori} is the specific enthalpy of the mixture that goes through the nozzle.

A proper prediction of the heat losses is extremely important for high accuracy combustion analysis. The starting point for the majority of 0D heat losses model is the Reynolds-Nusselt correlation for turbulent flow in pipes [62]. In the literature, the Woschni correlation [63] is the most extensively used for estimating the heat transfer coefficient prediction, and has been selected for the current study. It is important to highlight that in the case of the PCSI system, the energy analysis during the motoring tests is not only affected by the heat transfer losses (as in a standard engine if blow-by losses are neglected), but also by the mass exchange between both chambers. Therefore, the adjustment of the Woschni constants can only be performed once the discharge coefficient of the orifices is calibrated.

In the case of the pre-chamber can be adapted starting from equation 4.1:

$$HRR_{PC} = \frac{C_{P,PC}-R}{R} V_{PC} \frac{dP_{PC}}{dt} + \dot{Q}_{PC,loss} + \dot{m}_{ori} h_{ori} \tag{13}$$

where $C_{P,PC}$ is the constant pressure specific heat of the pre-chamber mixture, V_{PC} is the pre-chamber volume, dP_{PC} is the pressure derivative, $\dot{Q}_{PC,loss}$ is the heat transfer through the pre-chamber walls, and $\dot{m}_{ori}$ and h_{ori} is the mass flow rate and the specific enthalpy of the mixture that goes through the orifices.

In this case, the Woschni model has not been considered suitable for an accurate prediction of heat losses inside the pre-chamber since the characteristic velocity should not be directly linked to the mean piston speed, but to the velocity through the orifices. The pre-chamber flow field is controlled by the gas velocity through the nozzle (an order of magnitude bigger than the piston speed) which generates a high turbulence intensity that influences the convective heat exchange. Indeed, the Bargende correlation [48, 64] was slightly modified by Bardis et al. [44] for pre-chamber applications, and has been chosen for the heat losses estimation in the current work:

$$h_{B,PC} = \alpha_B \cdot V_{PC}^{-0.073} \cdot P_{PC}^{0.8} \cdot T_{PC}^{-0.53} \cdot u_{B,PC}^{0.78} \tag{14}$$

where the characteristic velocity is given by:

$$u_{B,PC} = \frac{1}{2}\sqrt{C_{B,k} \cdot \frac{8}{3}k + C_{B,u} \cdot u_{ori}^2} \tag{15}$$

$C_{B,k}$ and $C_{B,u}$ being two tuning constant for taking into account the velocity gradient inside the PC. Again, for the calculation of the heat transfer a wall temperature equal to the heating temperature of the RCEM (365 K) is assumed.

4.2. Pre-chamber flame propagation model.

Premixed turbulent flame speed is a critical parameter for the combustion analysis of PCSI engines simulations. By modeling the flame propagation as a function of the laminar flame speed, the turbulence intensity and the system geometry, it should be possible to create a model which yields predictive results even when individual parameters are changed [65].

First, an empirical correlation from Distaso et al. [66] is used for the laminar flame speed prediction depending on the equivalence ratio and the unburned mixture pressure and temperature:

$$S_L(\phi, T_u, P_u) = S_{L0} \left(\frac{T_u}{T_0}\right)^{\alpha} \left(\frac{p_u}{p_0}\right)^{\beta} \tag{16}$$

where α and β are a function of the equivalence ratio ϕ, and S_{L0} is the laminar flame speed at standard conditions ($p_0 = 1$atm, $T_0 = 298$K)

As a second step, the turbulent flame speed needs to be estimated as a function of the complex interaction between the initial laminar kernel with the turbulence field. This topic has been the focus of many different works in the literature, providing several correlations [67]. In this work, the correlation proposed by Kolla [54] has been used as the basis for the turbulent flame speed estimation:

$$\frac{S_T}{S_L} = \left\{ \left[b - a \left(1 + \left(\frac{u'}{S_L} \right)^{1.5} \left(\frac{\delta}{L_{pc}} \right)^{0.5} \right)^{-0.4} \right] \cdot \frac{T_{PC} - T_u}{T_u} \cdot \frac{L_{pc}}{\delta} \cdot \frac{u'}{S_L} + S_d \right\}^{0.5} \tag{17}$$

$$S_d = \frac{d}{\left(\frac{u'}{S_L} \right)^{0.75} + \left(\frac{\delta}{L_{pc}} \right)^{-0.25}} \cdot \left(\frac{u'}{S_L} \right)^{2.75} \tag{18}$$

where a, b and d are model constants, tuned for the used fuel and system layout. Furthermore, S_T depends on mean pre-chamber temperatures $(T_{PC})/(T_u)$ and turbulence key parameters as turbulent kinetic speed (u') [m/s]. Finally, the flame thickness (δ) is given by the Zeldovich-Blint correlation [68].

Finally, the mean expansion speed (U_B) can be estimated combining the turbulent flame speed with the mean gas speed (U_G), produced by the expansion of the hot combustion products, which can be evaluated once the heat release rate in the pre-chamber is known [62]. More specifically, the following relationships are used:

$$U_B = S_T + U_G \tag{19}$$

$$U_G = \frac{V_u}{\gamma_{PC} P_{PC} A_F} \cdot \frac{dP_{PC}}{dt} \tag{20}$$

$$A_F = \frac{\dot{m}_b}{\rho_u S_L} \tag{21}$$

where V_u and ρ_u are respectively the unburned mixture volume and density, A_F is the real flame surface and $\dot{m}_b$ is the burned mass flow rate, calculated from the instantaneous heat release rate and the lower heating value of the fuel, assuming a one-step combustion mechanism.

5. Results and discussion.

This section is focused on the experimental analysis of the pre-chamber combustion. First of all, the results are described in terms of the pressure evolution of both chambers and the mass flow exchanged between them. Later on, the same turbulence model described in section 3 is used to evaluate turbulent kinetic energy evolution in the pre-chamber during a combustion case. Based on this information, the heat release rate and the flame speed are evaluated. This flame speed is compared to the time elapsed from the spark for validation of the models used. Subsequently, the analysis is extended to other operating conditions in terms of the equivalence ratio in both chambers, showing consistent results.

5.1. Description of the baseline test.

Figure 9 shows the pressure evolution in the main combustion chamber (continuous line) and inside the pre-chamber (dotted line) as a function of the time elapsed from the beginning of the rapid compression for the baseline test, corresponding to a fuel-air equivalence ratio of 0.5 in the main chamber and 1.1 in the pre-chamber (at the spark activation time). In this graph, a vertical line shows the time at which the spark is discharged in the pre-chamber. During the compression stroke, and before the spark timing, the gases from the main chamber are pushed into the pre-chamber, filling it with the fuel-air mixture generated thanks to the fuel injection in the main chamber before the rapid compression.

The difference in the pressure between both chambers is mainly a consequence of the piston velocity and the pre-chamber geometrical details, especially the discharge coefficient of the orifices (a). Approximately after 14 ms from the test beginning, the auxiliary injection is made in the pre-chamber to reach the desired equivalence ratio in the pre-chamber at the spark timing (in the case of the figure, a fuel-air equivalence ratio of 1.1). Shortly after the spark activation, the pressure in the pre-chamber starts to increase as a consequence of the premixed combustion process (b). Once the pre-chamber pressure is higher than the one in the main chamber, hot gases are ejected through the pre-chamber orifices, acting as ignition sources for the main chamber lean mixture. Once the flame approaches the pre-chamber walls, the pressure starts to decrease, falling again below the main chamber pressure (which is rising due to the combustion already initiated) for a small portion of time, inducing a second filling process in the pre-chamber (c). Finally, during the expansion

stroke, the combustion products available in the pre-chamber are sucked into the main chamber (d).

Figure 10 shows the evolution of the velocity though the orifices and the turbulent kinetic energy, computed according to the zero-dimensional model introduced and validated in section 3. It is well known that for the PCSI system, the turbulence production and dissipation in the pre-chamber are strongly connected with the velocity and mass exchange through the orifices. Therefore, the maximum value of the TKE approximately coincides with the peak in the velocity between the orifices at the middle of the compression stroke. However, when the auxiliary injection is performed, the temperature inside the pre-chamber decreases due to fuel evaporation, slightly affecting the velocity and TKE evolution between 14.5ms and 16ms. Despite the RCEM piston and the nozzle velocity start to slow down, the TKE level at the Spark discharge instant (18 ms) is still high, ensuring a strong interaction between the initial flame kernel and the flow field. As the mass flow reverses (0.2 ms after spark timing -aST-), the main turbulence source is no longer applied, and the turbulence intensity quickly dissipates until the pre-chamber refilling. Once again, the mass flow revers during the expansion stroke and the turbulence extinguishes definitively under the second ejection. It is important to emphasize that the first ejection of gases reaches much higher velocity levels than the second one. Indeed, the two ejections will have a different impact on combustion development in the main chamber.

Figure 11 shows the heat release rate (continuous lines) and the heat losses (dotted lines) in both chambers (dark blue color for the main-chamber and light blue color for pre-chamber). This information is complemented by four pictures of specific stages of the main combustion event, obtained through the optical diagnostic described in 2. Until the spark activation, the energy balance between the heat losses through the walls and the exchanged gas enthalpy returns in a flat curve (almost equal to zero for both chambers), confirming that both models are properly calibrated. Once the spark is activated, after the induction time, the premixed combustion process in the pre-chamber takes place, leading to a rapid increase in the burned mass fraction and heat released. Moreover, as the average temperature increases in the pre-chamber volume, the heat losses become more relevant until the combustion process is mainly controlled by the ejection of the jets. The gray shading part highlights the start of the jets ejection in the main chamber, summarized by the 2 images on the top of fig.11 (t1 = 18.3 ms for the first jet, t2 = 18.6 ms for the last jet). Due to the system geometry and the spark plug position (fig. 2), the ejection from the pre-chamber

starts at slightly different instants for each orifice. The discharge from the pre-chamber continues until the flame approaches the pre-chamber walls and the combustion in the main chamber develops, resulting in a higher pressure in the main chamber. Once more, the re-filling takes place until TDC, which is shown in the bottom picture on the left with no ejection, leading to the second ejection during the expansion stroke (bottom picture on the right). Looking carefully at the phenomenon from the main chamber perspective, the first ejection marks the beginning of the combustion phase controlled by the hot turbulent jets coming from the pre-chamber. Once the PC mixture is burned the second combustion phase takes over, in which the flame propagation is considered self-sustained thanks to the MC turbulence enhanced. Indeed, during the first phase, most of the main chamber mixture is rapidly burned , while the heat release rate slows down during the second phase (around 19.6 ms) completing the combustion during the expansion phase.

Figure 12 shows the temporal evolution of the different terms for the predicted flame speed according to the model described in section 4 in terms of the time after the spark activation. This flame speed is analyzed up to the time at which the flame reaches the last of the pre-chamber orifices, according to a geometrical model based on the flame speed evolution and the pre-chamber layout. In this figure, the orange circled line represents the laminar flame speed S_L, estimated according to Distaso's correlation, which as it can be seen is around 0.4 m/s in the working conditions, and suffers a small increasing trend due to the unburned gas temperature increase induced by the compression. The red squared curve shows the evolution of the turbulent flame speed. Initially, this value is relatively low since the flame kernel after the spark discharge is still comparable to Taylor's macroscale, while an increasing trend appears later on due to the higher interaction between the flame and the turbulence field as the flame develops, leading to flame speed ratio values higher than 25. Then, the green squared line represents the mean gas speed U_G, which is maximum at the beginning of the combustion process where the volume of the burned products is small compared to the total pre-chamber volume. Finally, the blue dashed line shows the mean expansion speed U_B, calculated as the sum of the turbulent flame speed and the mean gas speed.

The estimated mean expansion speed can be validated taking into account the results from the combustion visualization. In particular, from the combustion images it is possible to detect the time at which the pre-chamber flame exits from each of the orifices. Then, a mean flame speed can be calculated taking into account the distance between the spark electrodes and the outlet section of each of these orifices (which is different due to the non-central location of the spark).

Considering this distance and the time calculated from the images, it is possible to calculate an equivalent mean expansion speed to be compared to the one computed by the 0D model. This information is available in Table 3, which shows an almost perfect matching between both values, which can be seen as a validation of the methodology used.

Orifice	**D[mm]**	**Time [ms]**	**Speed [m/s]**
1	4.99	0.43	11.6
2	5.14	0.43	11.9
3	7.34	0.49	15.0
4	7.57	0.55	13.8
5	9.43	0.63	15.0
6	9.54	0.69	13.8
U_B **(experimental)**			13.52 m/s
U_B **(0D model)**			13.54 m/s

Table 3: Mean expansion speed estimation from the visualization images and comparison with 0D model.

5.2. Equivalence ratio analysis.

As previously stated, the results shared so far correspond to a single condition characterized by an fuel/air equivalence ratio of 0.5 in the main chamber and 1.1 in the pre-chamber at the time of the spark activation. In the current section, the same methodology has been extended to different values of the two aforementioned conditions, in the ranges of 0.3-0.5 for the main chamber and 0.9-1.1 for the pre-chamber. Figure 13 shows the evolution of the pre-chamber equivalence ratio for three of these cases. In the left side, two cases of pre-chamber equivalence ratio at 1.1 but different main chamber one are compared. As it can be seen, the case at $\phi_{MC} = 0.5$ starts at a higher level due to the filling process during the compression stroke. At approximately 14 ms since the beginning of the rapid compression (87 mm piston position) the fuel injection in the pre-chamber starts, rapidly increasing the equivalence ratio from lean to rich conditions. Once the injection is finished, the pre-chamber filling continues until the desired equivalence ratio of 1.1 is reached at the spark activation time. In the right side of the figure, a similar evolution is seen, but in this case comparing the same main chamber equivalence ratio and two different targets in the pre-chamber: 0.9 and 1.1. Therefore, the most significant difference is induced by the duration of the fuel injection inside the pre-chamber.

Figure 14 shows the results in terms of the main chamber and pre-chamber pressure for the same cases previously analyzed. Again, in the left side the results for a same equivalence ratio in

the pre-chamber (1.1) but a different one in the main chamber (0.3 vs 0.5) are compared. Since the equivalence ratio in the pre-chamber is the same, the pressure increase in the pre-chamber during the premixed combustion process is very similar, within the expected cycle-to-cycle dispersion of such kind of combustion. This can be seen as a partial confirmation of the little effect of the fuel injection in the pre-chamber on the turbulence intensity and, therefore, on the combustion characteristics: the lower value of ϕ_{MC} is compensated by a higher injected fuel mass and longer injection duration, but no significant effects seems visible from combustion perspective. Instead, the pressure evolution in the main chamber once the combustion starts as a consequence of the hot gases ejection is very different for the two cases compared. Since the tests have been performed at same initial pressure and temperature (0.15 MPa and 365 K), the total air mass trapped in the cylinder is the same, so a change in the main chamber equivalence ratio means a change not only in the combustion propagation, but also in the total fuel energy available. Therefore, a faster and higher pressure rise is produced due to the higher amount of energy released.

The right hand side of the figure compares same main chamber equivalence ratio (0.5) but different conditions in the pre-chamber (ϕ_{PC} 0.9 and 1.1). In this case, a different piston position is recorded for the tests due to the pressure balance between the driving gas volume and the combustion chamber. As highlighted in previous chapters, the driving gas pushes the combustion piston, compressing the main chamber charge. As the pressure in the combustion chamber increases, the force produced is opposed to the driving gas pressure, braking the piston until the top dead center is reached. Due to the significantly different pressure evolution, the top dead center is slightly shifted for this two cases. Nevertheless, the piston position and therefore the ratio between the initial volume and the volume at the spark time activation is identical for both cases. The smaller equivalence ratio produces a larger induction time for the flame kernel, leading to a longer delay between the spark discharge and the pressure rise inside the pre-chamber. Again, the lower energy available in the pre-chamber combined with the slower flame speed produced at lean mixture leads to a slower pressure rise. As a consequence, the ejection from the pre-chamber will start later and at lower velocities, impacting the combustion in the main chamber despite, in this case, the equivalence ratio (and therefore the fuel energy available) is the same.

Figure 15 shows the same data in terms of the heat release rate and heat losses in the pre-chamber, computed according to the methodology described in section 4. The left chart confirms what was already discussed for figure 14: as long as the equivalence ratio in the pre-chamber is

matched, the combustion evolution is practically equal, within the expected variability of the test. Only a slight difference is seen in the second combustion event observed after 19.5 ms. This second combustion is a consequence of a refilling processes from the main chamber, once the pressure increased due to the main combustion exceeds the one in the pre-chamber. In this case, since the pressure rise and gas composition vary as a consequence of the different ϕ_{MC}, a more intense second combustion event is seen for the case of $\phi_{MC} = 0.5$. However, when the equivalence ratio is reduced in the pre-chamber (right side) the deterioration in the flame speed coupled with the lower energy available produce a less intense heat release rate, driving the overall combustion performance. Furthermore, a significant reduction of the heat losses is observed due to the reduced average combustion temperature and heat transfer coefficient.

Finally, the flame speed model can be applied to the different cases previously mentioned. These data is seen in terms of the mean expansion speed in Table 5, again in comparison with the same value computed from the combustion visualization data. First, it can be seen how the 0D model properly catches the experimental values in the ranges covered during the experimental campaign. Then, the values obtained confirm the expectations from the pressure and heat release rate data: the mean expansion speed is very similar when comparing the same equivalence ratio in the pre-chamber, but is severely deteriorated once this values falls from 1.1 to 0.9. This deterioration is coming from two sources: on the one hand, the lower equivalence ratio results in a lower pressure rise in the pre-chamber as a consequence of the lower energy available, reducing the mean gas speed; on the other hand, the smaller energy released results in a lower temperature inside the pre-chamber (for both burned and unburned zones) as combustion develops, affecting both laminar and turbulent speeds.

ϕ_{MC} [-]	ϕ_{PC}[-]	$U_{B,OD}$ [m/s]	$U_{B,exp}$ [m/s]
0.5	1.1	13.54	13.52
0.5	0.9	7.85	7.6
0.3	1.1	12.82	12.89
0.3	0.9	7.22	7.17

Table 4: Mean expansion speed estimation as a function of ϕ_{MC} and ϕ_{PC}.

In addition, taking into account that the existence of multiple correlations for the prediction of the turbulent flame speed is widely accepted in the literature, Kolla's model has been compared with the others correlations proposed by several authors such as Peters [69], Ronney [70], Klimov

[71], Gülder [72]. The calibration coefficients of all correlations have been adjusted in order to obtain near 0% error for the baseline case, and then the models validation have been extended for the remaining experimental cases.

	ϕ_{MC} - ϕ_{PC}			
	0.5 - 1.1	0.5 - 0.9	0.3 - 1.1	0.3 - 0.9
Ronney [m/s]	13.50	9.93	12.05	9.78
Klimov [m/s]	13.53	10	12.24	10.97
Gülder [m/s]	13.51	10.67	12.35	11.37
Peters [m/s]	13.51	10.14	12.17	10.81
Kolla [m/s]	13.54	7.85	12.82	7.22
Experimental [m/s]	13.52	7.6	12.89	7.17

Table 5: Mean expansion speed estimation as a function of ϕ_{MC} and ϕ_{PC}.

As the table 5 shows, the Kolla model is the only one able to guarantee high flexibility (low deviation from the experimental cases) when changing the boundary conditions (especially for the pre-chamber equivalence ratio). All the other correlations lead to a big error in the mean expansion speed prediction.

Finally, the flame speed results are represented in a classical Borghi diagram [73] thanks to the data extracted from the 0D turbulence model (Figure 16). In this diagram, the X-axis represents the ratio of Taylor's macroscale and the laminar flame thickness (estimated from the laminar flame speed and the mixture thermal diffusivity), while the Y-axis shows the ratio of the turbulence intensity and the laminar flame speed. The data is shown taking into account the temporal evolution up to the time at which the flame reaches the pre-chamber orifices. It can be concluded that the combustion inside the pre-chamber is in the thickened wrinkled flames regime, which is typical for spark-ignition operation. However, the data shows that the values of Damköhler number reached are in the range of 40, which combined with relatively high turbulence intensity, explain the very high flame speed ratio observed during the discussion of figure 12.

6. Conclusions.

In the current paper, a methodology based on the zero-dimensional modeling of the turbulence characteristics is proposed for the analysis of a stratified pre-chamber ignition system in a Rapid Compression-Expansion Machine. The model is first matched to the turbulent kinetic energy results from 3D-CFD simulations for motoring conditions, and then used to estimate the turbulent flame

speed evolution. This information is combined with the heat release rate computed from the analysis of the instantaneous pressure evolution for a comprehensive analysis of the combustion evolution in the pre-chamber. Finally, a broadband chemiluminescence visualization technique has been used to evaluate the flame transition from the pre-chamber to the rest of the cylinder.

The following conclusions can be drawn from the study:

- The turbulence evolution inside the pre-chamber during motoring tests can be properly captured by means of a $K-k-\epsilon$ model. A sensitivity analysis of this model shows that the most relevant parameters for a specific pre-chamber layout are:

    1. The proportion of the kinetic energy from the filling flow that is transfered to turbulent kinetic energy (a_{in}).
    2. A scaling factor for the turbulence dissipation (C_ϵ).

- In a stratified pre-chamber ignition system, the evolution of the pressures in the pre-chamber and main chamber shows three phases after the spark discharge:

    1. As the combustion in the pre-chamber develops, the pressure increases inducing the ejection of hot gases into the main chamber, initiating the main combustion. The heat release rate in the pre-chamber in this first stage can be adjusted by a proper control of the equivalence ratio, regardless the conditions in the rest of the cylinder.
    2. After some time, a decay in the heat release rate in the pre-chamber is seen as the flame approaches the pre-chamber walls, while the combustion in the main chamber continues. This leads to a moment at which the main chamber pressure rises over the one in the pre-chamber, stopping the ejection and initiating a re-filling process of the pre-chamber with unburned gases. This re-filling is stronger as the equivalence ratio in the main chamber increases.
    3. The combustion of the gases entering the pre-chamber during the re-filling can produce a second ejection and combustion in the main chamber during the expansion stroke, but at a much lower rate than the first one.

- The mean expansion speed, calculated as the combined contribution of the turbulent flame speed and the gas expansion process, is validated against the time needed for the flame

to reach each of the pre-chamber orifices, obtained from the broadband chemiluminescence images, with a maximum variation of 0.2 m/s.

- The flame speed is very consistent as long as the equivalence ratio in the pre-chamber is maintained, while a decrease of almost 40% is achieved when going from slightly rich ($\phi_{PC} = 1.1$) to lean $\phi_{PC} = 0.9$ operation. This decrease is more significant than expected due to the fact that the equivalence ratio is controlled by the fuel quantity, severely impacting the energy balance and maximum temperature reached inside the pre-chamber.
- The analysis of pre-chamber flame speed and turbulence characteristics in a Borghi diagram confirms a thickened wrinkled flames regime, characterized by Damköhler number values in the range of 40 and flame speed ratio values higher than 25.

Acknowledgments.

The authors would like to thank the collaboration of Mr. Omar Huerta and Mr. Santiago Caro during the experimental campaign. The authors would also like to thank the computer resources, technical expertise and assistance provided by Universitat Politècnica de València in the use of the super-computer "Rigel".

Nomenclature

a	Kolla's model tuning constant 1	
A_f	Real flame area	m^2
A_{ori}	Orifice Surface	m^2
A_{PC}	Pre-chamber surface	m^2
b	Kolla's model tuning constant 2	
C_β	Coefficient for turbulence production inside the pre-chamber by the mean kinetic energy flow field	
C_ϵ	Fraction of incoming turbulence kinetic energy dissipated	

$C_{B,k}$	Tuning constant for the Bargende heat transfer characteristic velocity scaling the pre chamber turbulence	
$C_{B,u}$	Tuning constant for the Bargende heat transfer characteristic velocity scaling the nozzle velocity	
$C_{d,dis}$	Orifice discharge coefficient during the pre-chamber discharge process	
$C_{d,fil}$	Orifice discharge coefficient during the pre-chamber filling process	
C_d	Orifice discharge coefficient	
C_{len}	Model tuning coefficient for the turbulence macroscale	
$C_{P,MC}$	Specific heat constant under constant pressure of the main chamber mixture	$\frac{J}{molK}$
$C_{P,PC}$	Specific heat constant under constant pressure of the pre-chamber mixture	$\frac{J}{molK}$
C_T	Pre-chamber geometric coefficient	
COV	Coefficient of variation	
d	Kolla's model tuning constant 3	
D_{ori}	Orifice diameter	m
$F_{w\epsilon}$	Turbulent dissipation flux to the walls	$\frac{Kgm^2}{s^4}$
F_{wk}	Turbulence kinetic energy flux to the walls	$\frac{Kgm^2}{s^3}$
$h_{B,PC}$	Heat transfer coefficient for the pre-chamber according to Bargende's correlation	$\frac{w}{m^2K}$
h_{ori}	Specific enthalpy the interchanged gas mixture	$\frac{J}{mol}$
HRR_{MC}	Main chamber heat release rate	W
HRR_{PC}	Pre-chamber heat release rate	W
ICE	Internal combustion engine	
K	Mass averaged mean kinetic energy in the pre-chamber	$\frac{m^2}{s^2}$
L_{PC}	Taylor's macroscale in the pre-chamber	m

$\dot{m}_b$	Pre-chamber burned mixture mass flow rate	$\frac{Kg}{s}$
$\dot{m}_{ori}$	Mass flow rate through the nozzle orifices	$\frac{Kg}{s}$
m_{PC}	Pre-chamber mass	kg
MC	Main chamber	
n_{ori}	Number of orifices	
P_ϵ	Turbulence kinetic energy dissipation rate in the pre-chamber by the mean velocity field	$\frac{Kgm^2}{s^4}$
p_{in}	Pressure at nozzle inlet	MPa
P_{kl}	Turbulence kinetic energy production rate in the pre-chamber by the mean velocity field	$\frac{Kgm^2}{s^3}$
P_{MC}	Main chamber pressure	MPa
p_{out}	Pressure at nozzle outlet	MPa
P_{PC}	Pre-chamber pressure	MPa
P_{sw}	Turbulence kinetic energy production rate in the pre-chamber by the swirling flow	$\frac{Kgm^2}{s^3}$
$P_{u\epsilon}$	Mass averaged turbulence dissipation rate in the pre-chamber	$\frac{Kgm^2}{s^4}$
P_{uK}	Mean kinetic energy production rate in the pre-chamber	$\frac{Kgm^2}{s^3}$
P_{uk}	Mass averaged turbulence kinetic energy rate incoming in the pre-chamber	$\frac{Kgm^2}{s^3}$
P_u	Pre-chamber unburned mixture pressure	K
PC	Pre-chamber	
$PCSI$	Pre-chamber spark ignition	
$\dot{Q}_{MC,loss}$	Main chamber heat losses	W
$\dot{Q}_{PC,loss}$	Pre-chamber heat losses	W

$RCEM$	Rapid compression-expansion machine	
RCM	Rapid compression machine	
Re	Nozzle Reynolds number	
S_{L0}	Laminar flame speed at room conditions	$\frac{m}{s}$
S_L	Laminar flame speed	$\frac{m}{s}$
S_T	Turbulent flame speed	$\frac{m}{s}$
SOT	Start of the test	
T_{MC}	Averaged main chamber mixture temperature	K
$T_{PC,wall}$	Averaged main chamber walls temperature	K
T_{PC}	Averaged pre-chamber mixture temperature	K
T_{PC}	Averaged pre-chamber walls temperature	K
T_u	Pre-chamber unburned mixture temperature	K
TDC	Top dead center	
u'	Pre-chamber turbulence kinetic velocity	$\frac{m}{s}$
$u_{B,PC}$	Characteristic heat transfer velocity of the pre-chamber according to Bargende's correlation	$\frac{m}{s}$
U_B	Mean expansion speed	$\frac{m}{s}$
U_G	Mean gas speed	$\frac{m}{s}$
u_{ori}	Velocity through the nozzle orifices	$\frac{m^2}{s^2}$
V_{MC}	Main chamber volume	m^3
V_{PC}	Pre-chamber volume	m^3
V_u	Pre-chamber unburned mixture volume	m^3

α	Temperature influence exponent in Distaso's correlation	
α_B	Bargende model scaling factor	
α_{in}	Fraction of incoming kinetic energy converted to turbulence	
β	Pressure influence exponent	
δ	Laminar flame thickness	m
ϵ	Mass averaged turbulence dissipation rate in the pre-chamber	$\frac{m^2}{s^3}$
γ_{PC}	Pre-chamber mixture heat capacity ratio	
ν	Turbulent viscosity in the pre-chamber	$\frac{m^2}{s}$
ϕ	Equivalence ratio	
$\dot{\rho}_{pc}$	Temporal derivative of the average pre-chamber charge density	$\frac{Kg}{sm^3}$
ρ_{in}	Density at nozzle inlet	$\frac{Kg}{m^3}$
ρ_{pc}	Average pre-chamber charge density	$\frac{Kg}{m^3}$
ρ_u	Pre-chamber unburned mixture density	$\frac{Kg}{m^3}$

References

[1] P. L. Kinney, Interactions of climate change, air pollution, and human health, Current environmental health reports 5 (1) (2018) 179–186.

[2] L. Postrioti, S. Malaguti, M. Bosi, G. Buitoni, S. Piccinini, G. Bagli, Experimental and numerical characterization of a direct solenoid actuation injector for Diesel engine applications, Fuel 118 (2014) 316–328. doi:10.1016/j.fuel.2013.11.001.
URL http://dx.doi.org/10.1016/j.fuel.2013.11.001

[3] R. Payri, J. De la Morena, V. Pagano, A. Hussain, G. Sammut, L. Smith, One-dimensional modeling of the interaction between close-coupled injection events for a ballistic solenoid injector, International Journal of Engine Research (2018). doi:10.1177/1468087418760973.

[4] F. Salvador, J. De la Morena, J. Martínez-López, D. Jaramillo, Assessment of compressibility effects on internal nozzle flow in diesel injectors at very high injection pressures, Energy Conversion and Management 132 (2017). doi:10.1016/j.enconman.2016.11.032.

[5] R. Payri, F. Salvador, J. De la Morena, V. Pagano, Experimental investigation of the effect of orifices inclination angle in multihole diesel injector nozzles. Part 2 - Spray characteristics, Fuel (2017). doi:10.1016/j.fuel.2017.07.076.

[6] L. Araneo, R. Donde', Flash boiling in a multihole G-DI injector – Effects of the fuel distillation curve, Fuel 191 (2017) 500–510. doi:10.1016/j.fuel.2016.11.104.
URL http://dx.doi.org/10.1016/j.fuel.2016.11.104

[7] R. Banerjee, S. Kumar, Numerical investigation of stratified air/fuel preparation in a GDI engine, Applied Thermal Engineering 104 (2016) 414–428. doi:10.1016/j.applthermaleng.2016.05.050.
URL http://dx.doi.org/10.1016/j.applthermaleng.2016.05.050

[8] P. Sphicas, L. M. Pickett, S. A. Skeen, J. H. Frank, Inter-plume aerodynamics for gasoline spray collapse, International Journal of Engine Research 19 (10) (2018) 1048–1067.

[9] W. Zeng, M. Sjöberg, D. L. Reuss, Z. Hu, The role of spray-enhanced swirl flow for combustion stabilization in a stratified-charge DISI engine, Combustion and Flame 168 (x) (2016) 166–185. doi:10.1016/j.combustflame.2016.03.015.

[10] B. Peterson, E. Baum, A. Dreizler, B. Böhm, An experimental study of the detailed flame transport in a si engine using simultaneous dual-plane oh-lif and stereoscopic piv, Combustion and Flame 202 (2019) 16 – 32. doi:https://doi.org/10.1016/j.combustflame.2018.12.024.
URL http://www.sciencedirect.com/science/article/pii/S0010218018305418

[11] E. Mancaruso, C. Perozziello, L. Sequino, B. M. Vaglieco, Characterization of pure and blended biodiesel spray in a compression ignition engine by means of advanced diagnostics and 1D model, Fuel 239 (2019) 1102–1114. doi:10.1016/j.fuel.2018.11.099.
URL https://doi.org/10.1016/j.fuel.2018.11.099

[12] R. Payri, F. J. Salvador, J. De La Morena, V. Pagano, Using a one-dimensional spray model to improve liquid length and ignition delay estimations for diesel flames, Applied Thermal Engineering 124 (2017) 1090–1102. doi:10.1016/j.applthermaleng.2017.06.102.
URL http://dx.doi.org/10.1016/j.applthermaleng.2017.06.102

[13] Y. Ling, D. Fuster, G. Tryggvason, S. Zaleski, G. Tryggvason, S. Zaleski, A two-phase mixing layer between parallel gas and liquid streams: multiphase turbulence statistics and influence of interfacial instability, Journal of Fluid Mechanics 859 (2019) 268–307. arXiv:arXiv:1808.01996v1, doi:10.1017/jfm.2018.825.
URL https://www.cambridge.org/core/product/identifier/S002211201800825X/type/journal{_}article

[14] A. Umemura, J. Shinjo, Detailed SGS atomization model and its implementation to two-phase flow LES, Combustion and Flame 195 (2018) 232–252. doi:10.1016/j.combustflame.2018.01.026.
URL https://doi.org/10.1016/j.combustflame.2018.01.026

[15] J. Manin, Numerical investigation of the primary breakup region of high-pressure sprays, Atomization and Sprays 28 (12) (2019) 1081–1100. doi:10.1615/AtomizSpr.2019026990.
URL http://dl.begellhouse.com/journals/6a7c7e10642258cc,forthcoming,26990.html

[16] F. J. Salvador, S. Ruiz, M. Crialesi-Esposito, I. Blanquer, Analysis on the Effects of Turbulent Inflow Conditions on Spray Primary Atomization in the Near-Field by Direct Numerical Simulation, International Journal of Multiphase Flow 102 (2018) 49–63. doi:10.1016/j.ijmultiphaseflow.2018.01.019.
URL http://linkinghub.elsevier.com/retrieve/pii/S0301932217305037

[17] T. D. Fansler, S. E. Parrish, Spray measurement technology: a review, Measurement Science and Technology 26 (1) (2015) 012002. doi:10.1088/0957-0233/26/1/012002.
URL http://stacks.iop.org/0957-0233/26/i=1/a=012002?key=crossref.a51a57d78742e5d88aea3d6f06688efc

[18] T. Xuan, J. M. Desantes, J. V. Pastor, J. M. Garcia-Oliver, Soot temperature characterization

of spray a flames by combined extinction and radiation methodology, Combustion and Flame 204 (March) (2019) 290–303. doi:10.1016/j.combustflame.2019.03.023.

[19] R. Payri, J. De La Morena, J. Monsalve-Serrano, F. C. Pesce, A. Vassallo, Impact of counter-bore nozzle on the combustion process and exhaust emissions for light-duty diesel engine application, International Journal of Engine Research 20 (1) (2019) 46–57. doi:10.1177/1468087418819250.

[20] M. Yao, Z. Zheng, H. Liu, Progress and recent trends in homogeneous charge compression ignition (HCCI) engines, Progress in Energy and Combustion Science 35 (5) (2009) 398–437. doi:10.1016/j.pecs.2009.05.001.
URL http://dx.doi.org/10.1016/j.pecs.2009.05.001

[21] J. V. Pastor, J. M. Garcia-Oliver, A. Garcia, C. Micó, R. P. Durrett, A spectroscopy study of gasoline partially premixed compression ignition spark assisted combustion, Applied Energy 104 (2013) 568–575. doi:10.1016/j.apenergy.2012.11.030.
URL http://dx.doi.org/10.1016/j.apenergy.2012.11.030

[22] E. Mancaruso, B. M. Vaglieco, Spectroscopic analysis of the phases of premixed combustion in a compression ignition engine fuelled with diesel and ethanol, Applied Energy 143 (2015) 164–175. doi:10.1016/j.apenergy.2015.01.031.

[23] Y. Sakai, K. Kunii, S. Tsutsumi, Y. Nakagawa, Combustion characteristics of the torch ignited engine, SAE Technical Paper (1974).

[24] A. A. Quader, Lean combustion and the misfire limit in spark ignition engines, SAE Technical Paper (1974).

[25] K. Kornbluth, J. Greenwood, Z. McCaffrey, D. Vernon, P. Erickson, Extension of the lean limit through hydrogen enrichment of a lfg-fueled spark-ignition engine and emissions reduction, International Journal of Hydrogen Energy 35 (3) (2010) 1412–1419.

[26] T. D. Fansler, D. L. Reuss, V. Sick, R. N. Dahms, Invited review: Combustion instability in spray-guided stratified-charge engines: A review, International Journal of Engine Research 16 (3) (2015) 260–305.

[27] T. Kitagawa, T. Nakahara, K. Maruyama, K. Kado, A. Hayakawa, S. Kobayashi, Turbulent burning velocity of hydrogen–air premixed propagating flames at elevated pressures, International Journal of Hydrogen Energy 33 (20) (2008) 5842–5849.

[28] M. Hunzinger, S. Merkel, A. Nauwerck, A. Velji, U. Spicher, Turbulent flame propagation with cold walls during lean combustion in si-engines, SAE Technical Paper (2005).

[29] D. Dunn-Rankin, Lean combustion: technology and control, Academic Press, 2011.

[30] E. Toulson, H. J. Schock, W. P. Attard, A review of pre-chamber initiated jet ignition combustion systems, SAE Technical Paper (2010).

[31] W. P. Attard, P. Parsons, A normally aspirated spark initiated combustion system capable of high load, high efficiency and near zero nox emissions in a modern vehicle powertrain, SAE International Journal of Engines 3 (2) (2010) 269–287.

[32] W. P. Attard, H. Blaxill, A single fuel pre-chamber jet ignition powertrain achieving high load, high efficiency and near zero nox emissions, SAE International Journal of Engines 5 (3) (2012) 734–746.

[33] W. P. Attard, P. Parsons, Flame kernel development for a spark initiated pre-chamber combustion system capable of high load, high efficiency and near zero nox emissions, SAE International Journal of Engines 3 (2) (2010) 408–427.

[34] J. G. C. Baeta, F. A. Rodrigues Filho, M. Pontoppidan, R. M. Valle, T. R. V. da Silva, Exploring the performance limits of a stratified torch ignition engine using numerical simulation and detailed experimental approaches, Energy conversion and management 126 (2016) 1093–1105.

[35] M. Bunce, H. Blaxill, Methodology for combustion analysis of a spark ignition engine incorporating a pre-chamber combustor, SAE Technical Paper (2014).

[36] B. Korb, K. Kuppa, H. D. Nguyen, F. Dinkelacker, G. Wachtmeister, Experimental and numerical investigations of charge motion and combustion in lean-burn natural gas engines, Combustion and Flame 212 (2020) 309–322.

[37] A. Jamrozik, W. Tutak, A. Kociszewski, M. Sosnowski, Numerical simulation of two-stage combustion in si engine with prechamber, Applied Mathematical Modelling 37 (5) (2013) 2961–2982.

[38] M. Gholamisheeri, B. C. Thelen, G. R. Gentz, I. S. Wichman, E. Toulson, Rapid compression machine study of a premixed, variable inlet density and flow rate, confined turbulent jet, Combustion and Flame 169 (2016) 321–332.

[39] J. M. Desantes, R. Novella, J. De La Morena, V. Pagano, Achieving ultra-lean combustion using a pre-chamber spark ignition system in a rapid compression-expansion machine, SAE Technical Paper (2019).

[40] G. Gentz, B. Thelen, P. Litke, J. Hoke, E. Toulson, Combustion visualization, performance, and cfd modeling of a pre-chamber turbulent jet ignition system in a rapid compression machine, SAE International Journal of Engines 8 (2) (2015) 538–546.

[41] G. Gentz, B. Thelen, M. Gholamisheeri, P. Litke, A. Brown, J. Hoke, E. Toulson, A study of the influence of orifice diameter on a turbulent jet ignition system through combustion visualization and performance characterization in a rapid compression machine, Applied Thermal Engineering 81 (2015) 399–411.

[42] M. Gholamisheeri, B. Thelen, G. Gentz, E. Toulson, Cfd modeling of an auxiliary fueled turbulent jet ignition system in a rapid compression machine, SAE Technical Paper (2016).

[43] M. Gholamisheeri, I. S. Wichman, E. Toulson, A study of the turbulent jet flow field in a methane fueled turbulent jet ignition (TJI) system, Combustion and Flame 183 (2017) 194–206. doi:10.1016/j.combustflame.2017.05.008.

[44] K. Bardis, G. Xu, P. Kyrtatos, Y. M. Wright, K. Boulouchos, A zero dimensional turbulence and heat transfer phenomenological model for pre-chamber gas engines, SAE Technical Paper (2018).

[45] N. Fogla, M. Bybee, M. Mirzaeian, F. Millo, S. Wahiduzzaman, Development of a k-k-e phenomenological model to predict in-cylinder turbulence, SAE International Journal of Engines 10 (2) (2017) 562–575.

[46] C. Borgnakke, G. Davis, R. Tabaczynski, Predictions of in-cylinder swirl velocity and turbulence intensity for an open chamber cup in piston engine, SAE Transactions (1981) 964–978.

[47] M. Achuth, P. S. Mehta, Predictions of tumble and turbulence in four-valve pentroof spark ignition engines, International Journal of Engine Research 2 (3) (2001) 209–227.

[48] M. Bargende, Ein Gleichungsansatz zur Berechnung der instationären Wandwärmeverluste im Hochdruckteil von Ottomotoren, na, 1990.

[49] I. W. S. L. Cruz, C. E. C. Alvarez, A. F. Teixeira, R. M. Valle, Zero-dimensional mathematical model of the torch ignited engine, Applied Thermal Engineering 103 (2016) 1237–1250. doi:10.1016/j.applthermaleng.2016.05.017.
URL http://dx.doi.org/10.1016/j.applthermaleng.2016.05.017

[50] K. Hiraoka, K. Nomura, A. Yuuki, Y. Oda, T. Kameyama, Phenomenological 0-dimensional combustion model for spark-ignition natural gas engine equipped with pre-chamber, SAE Technical Paper (2016).

[51] F. Bozza, V. De Bellis, D. Tufano, E. Malfi, C. Müller, K. Habermann, A quasi-dimensional model of pre-chamber spark-ignition engines, SAE Technical Paper (2019).

[52] M. Baratta, A. Catania, E. Spessa, A. Vassallo, Development of an improved fractal model for the simulation of turbulent flame propagation in si engines, SAE Technical Paper (2005).

[53] G. Xu, M. Kotzagianni, P. Kyrtatos, Y. M. Wright, K. Boulouchos, Experimental and numerical investigations of the unscavenged prechamber combustion in a rapid compression and expansion machine under engine-like conditions, Combustion and Flame 204 (2019) 68–84.

[54] H. Kolla, J. W. Rogerson, N. Swaminathan, Validation of a turbulent flame speed model across combustion regimes, Combustion Science and Technology 182 (3) (2010) 284–308. doi:10.1080/00102200903341587.

[55] J. M. Desantes, J. J. López, S. Molina, D. López-Pintor, Theoretical development of a new procedure to predict ignition delays under transient thermodynamic conditions and validation using a rapid compression–expansion machine, Energy conversion and management 108 (2016) 132–143.

[56] R. Payri, F. Salvador, J. Gimeno, G. Bracho, A new methodology for correcting the signal cumulative phenomenon on injection rate measurements, Experimental techniques 32 (1) (2008) 46–49.

[57] CONVERGE is a trade mark of Convergent Science, https://convergecfd.com.

[58] R. Novella, J. Gomez-Soriano, P. J. Martinez-Hernandiz, C. Libert, Evaluation of the passive pre-chamber ignition concept for future high compression ratio turbocharged spark-ignition engines, Applied energy 248 (2019) 576–588.

[59] D. López-Pintor, Theoretical and experimental study on the autoignition phenomena of homogeneous reactive mixtures, Ph.D. thesis (2017).

[60] J. Martín, Contribución al diagnóstico de la combustión en motores Diesel de inyección directa, Ph.D. thesis, Universitat Politècnica de València (2007).

[61] I. Statgraphics Centurion XVII is a trademark of Statgraphics Technologies, http://www.statgraphics.com/.

[62] J. B. Heywood, Internal combustion engine fundamentals, Mcgraw-hill, 1988.

[63] G. Woschni, A universally applicable equation for the instantaneous heat transfer coefficient in the internal combustion engine, SAE Technical Paper (1967).

[64] M. Chiodi, M. Bargende, Improvement of engine heat-transfer calculation in the three-dimensional simulation using a phenomenological heat-transfer model, SAE Technical Paper (2001).

[65] S. Bjerkborn, Development and validation of a turbulent flame propagation model, Ph.D. thesis (2011).

[66] R. Amirante, E. Distaso, P. Tamburrano, R. D. Reitz, Laminar flame speed correlations for methane, ethane, propane and their mixtures, and natural gas and gasoline for spark-ignition engine simulations, International Journal of Engine Research 18 (9) (2017) 951–970. doi:10.1177/1468087417720018.

[67] E. M. Burke, F. Güthe, R. F. Monaghan, A comparison of turbulent flame speed correlations for hydrocarbon fuels at elevated pressures, 2016.

[68] R. J. Blint, The relationship of the laminar flame width to flame speed, Combustion Science and Technology 49 (1-2) (1986) 79–92.

[69] N. Peters, The turbulent burning velocity for large-scale and small-scale turbulence, Journal of Fluid mechanics 384 (1999) 107–132.

[70] P. D. Ronney, Some open issues in premixed turbulent combustion, in: Modeling in Combustion Science, Springer, 1995, pp. 1–22.

[71] A. Klimov, Premixed turbulent flames-interplay of hydrodynamic and chemical phenomena, Flames, Lasers, and Reactive Systems (1983) 133–146.

[72] Ö. L. Gülder, Turbulent premixed flame propagation models for different combustion regimes, in: Symposium (International) on Combustion, Vol. 23, Elsevier, 1991, pp. 743–750.

[73] R. Borghi, On the Structure and Morphology of Turbulent Premixed Flames. In: Casci C., Bruno C. (eds) Recent Advances in the Aerospace Sciences, Springer (Boston, MA, USA), 1985.

[74] G. Blesinger, R. Koch, H.-J. Bauer, Influence of flow field scaling on flashback of swirl flames, Experimental Thermal and Fluid Science 34 (3) (2010) 290–298.

Figures.

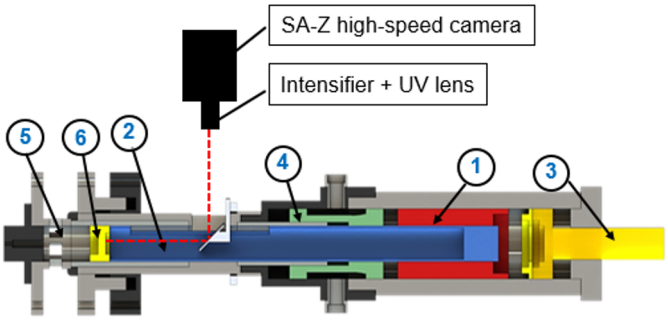

1	Pushing piston	4	Air piston
2	Driver piston	5	Combustion chamber
3	Displacement piston	6	Combustion piston

Figure 1: Rapid compression-expansion machine

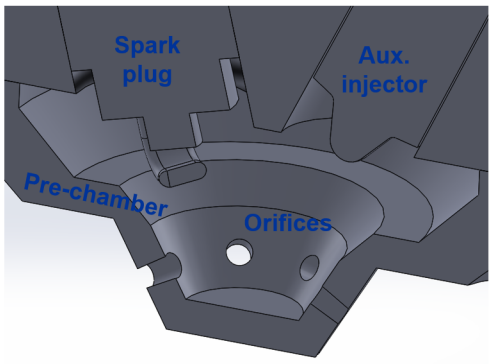

Figure 2: Pre-chamber Design

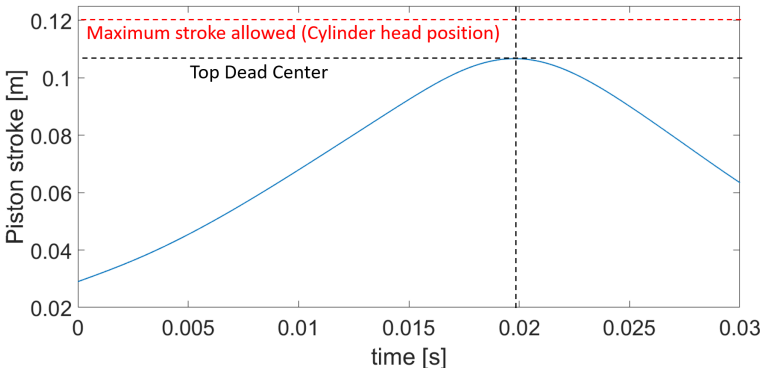

Figure 3: Experimental piston position under motoring conditions imposed to the 3D CFD simulations.

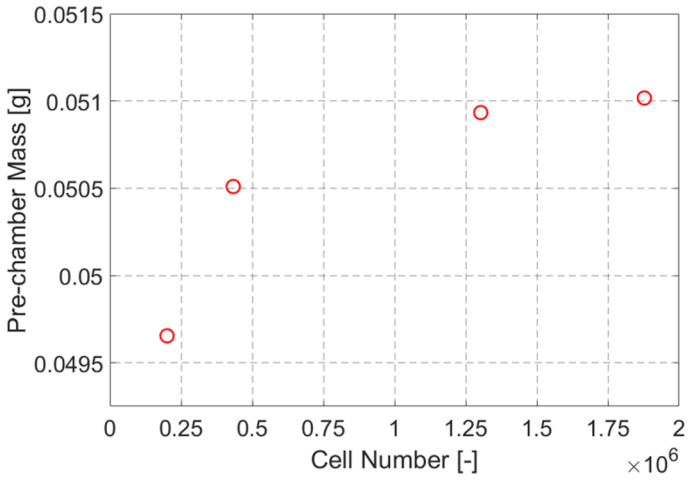

Figure 4: Results of mesh sensitivity analysis in terms of pre-chamber mass evolution during the compression stroke.

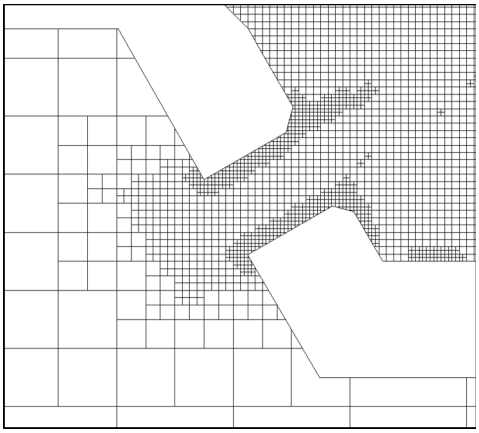

Figure 5: Structure of the final mesh around the orifice section close to top dead center.

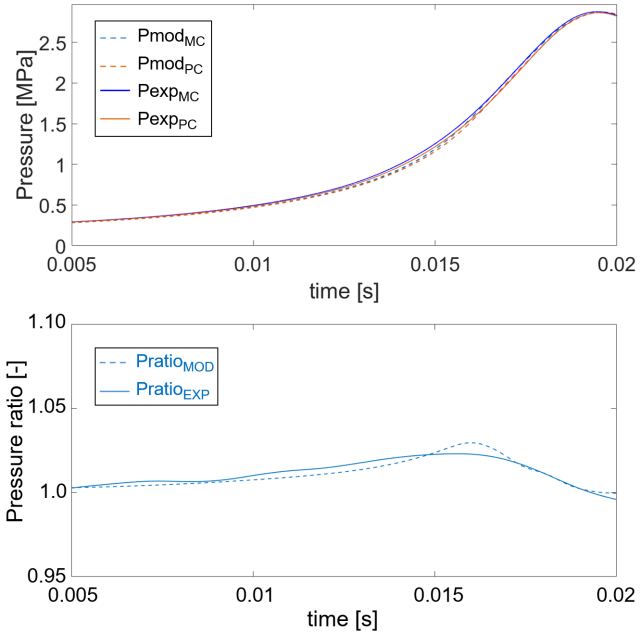

Figure 6: Validation of the CFD simulations in terms of: Pressure evolution in main-chamber (blue) and pre-chamber (orange) on the top. Pressure ratio (P_{MC}/P_{PC}) modelled (dashed) and experimental (continuous) on the bottom.

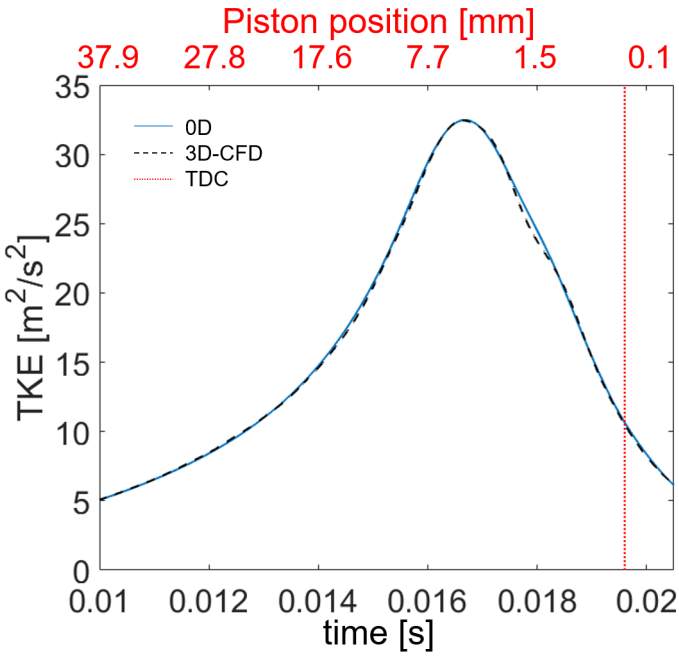

Figure 7: Comparison of 0D and 3D-CFD models in terms of turbulent kinetic energy evolution inside the pre-chamber during compression.

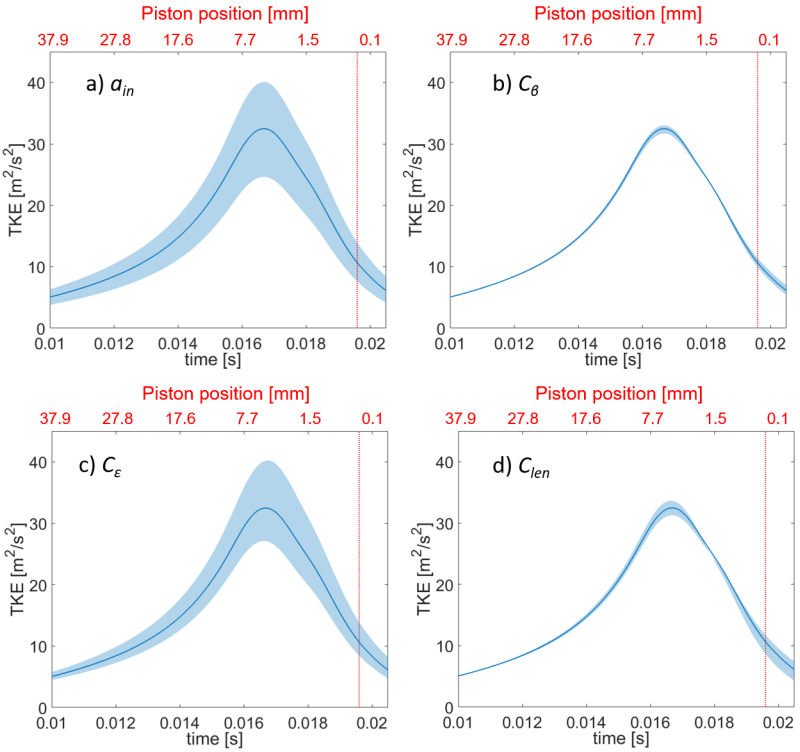

Figure 8: Sensitivity analysis of each model constant around the optimal solution.

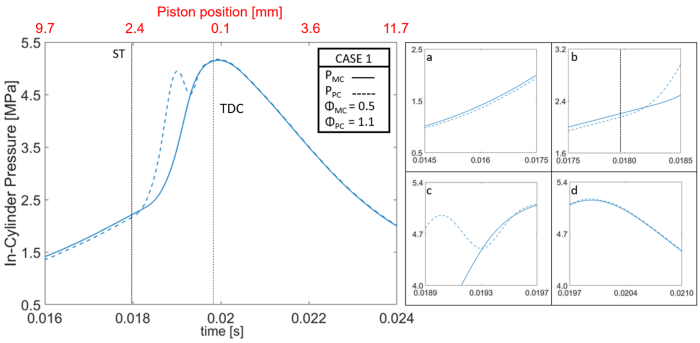

Figure 9: In-Cylinder pressure evolution:(a) Filling process. (b) Pre-chamber start of combustion (1st ejection). (c) Pre-chamber pressure peak and re-filling process. (d) 2nd ejection and pre-chamber emptying process

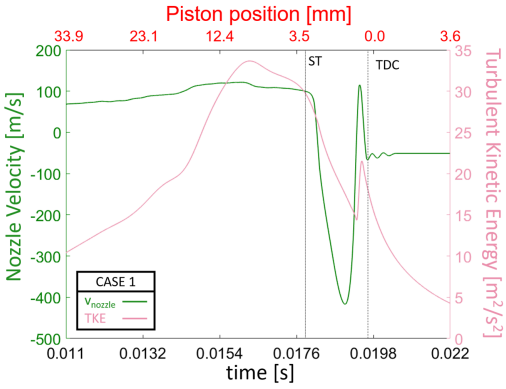

Figure 10: Turbulent Kinetic Energy and Nozzle velocity time evolutions.

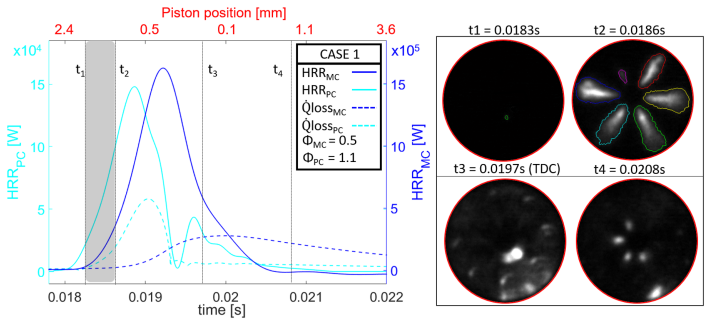

Figure 11: Left side: Heat Release Rate in both chambers. Right side: Combustion visualization images.

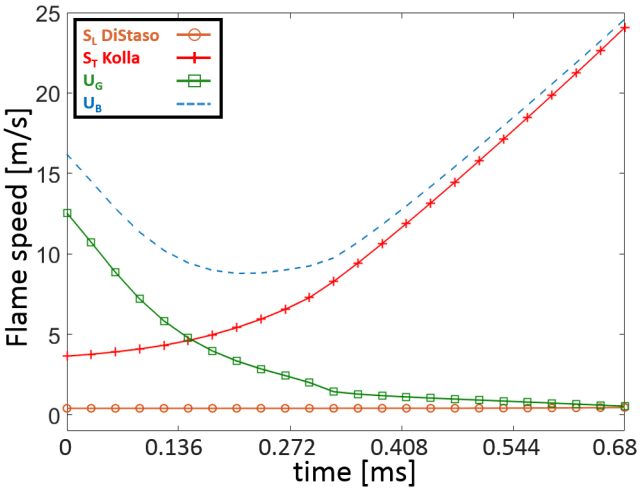

Figure 12: Instantaneous flame speed evaluation.

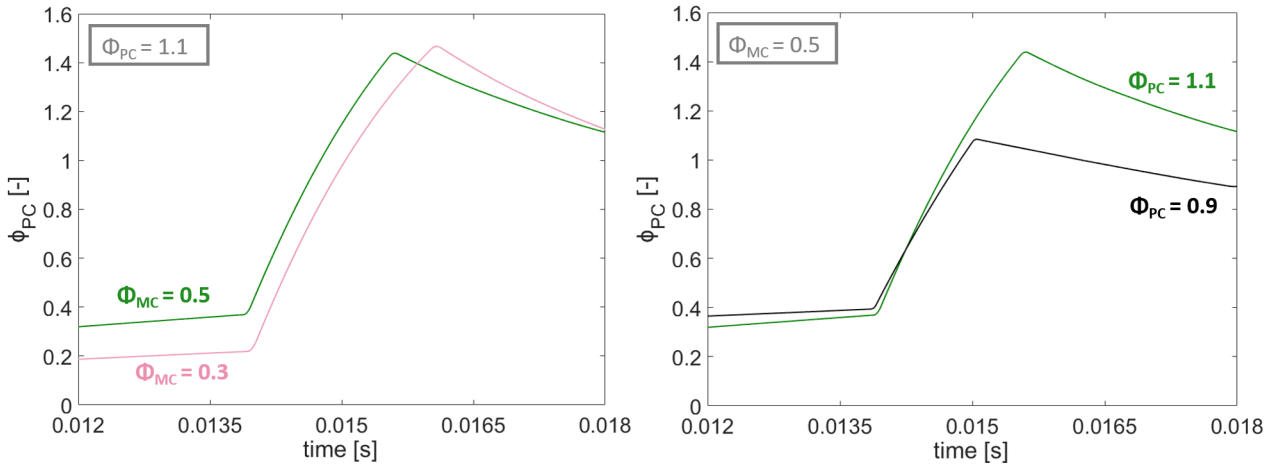

Figure 13: Time evolution of the pre-chamber equivalence ratio based on the 0D model.

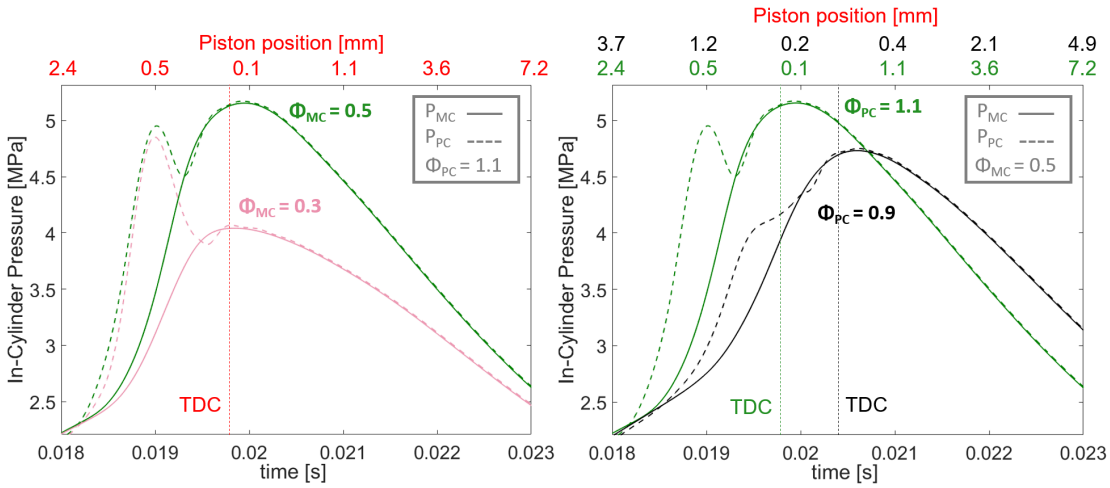

Figure 14: Instantaneous pressure evolution as a function of ϕ_{MC} (left) and ϕ_{PC} (right).

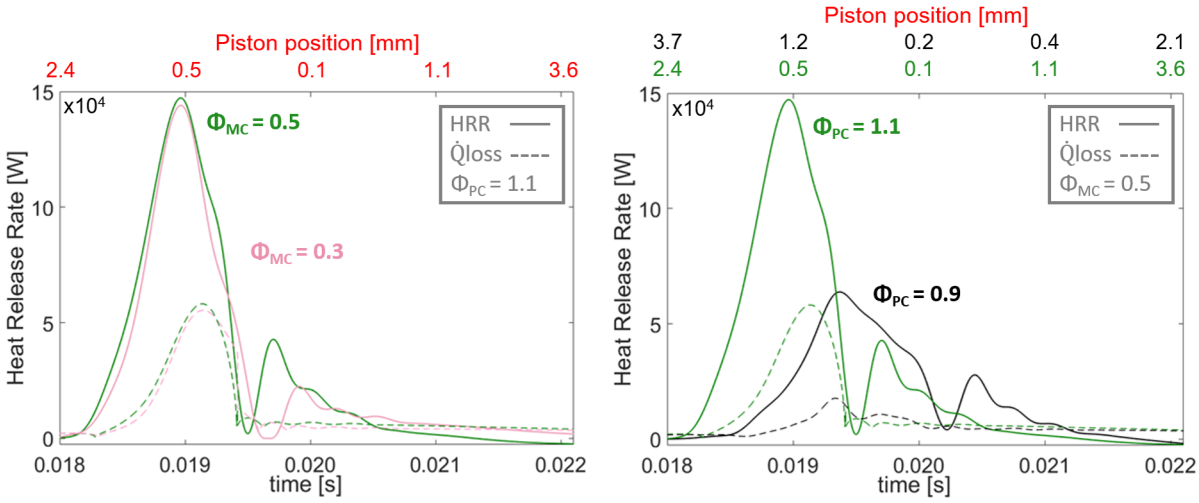

Figure 15: Heat release rate evolution as a function of ϕ_{MC} (left) and ϕ_{PC} (right).

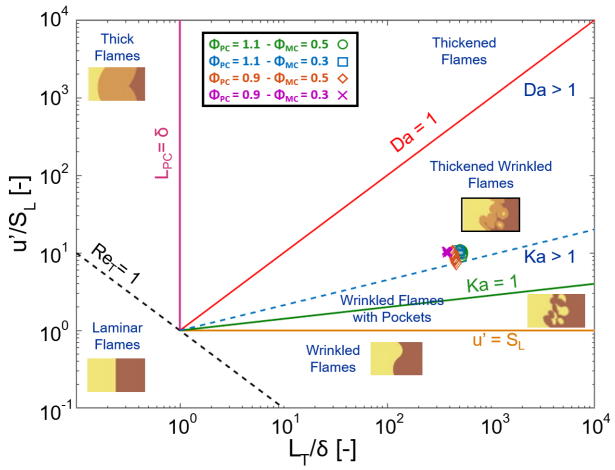

Figure 16: Borghi's diagram for turbulent flame regime as a function of ϕ_{MC} and ϕ_{PC} (turbulent flame schematic adapted from [74]).